Journal of Hydrology 596 (2021) 126097

Contents lists available at ScienceDirect

Journal of Hydrology

journal homepage: www.elsevier.com/locate/jhydrol

Research papers

Analytical solutions for contaminant fate and transport in parallel plate fracture-rock matrix systems with poiseuille flow

Junqi Huang [a,*], John Christ [b], Mark N. Goltz [c]

[a] Groundwater Characterization and Remediation Division, Center for Environmental Solutions and Emergency Response, U.S. EPA, Ada 74820 OK, USA
[b] S&B Christ Consulting, LLC., 9555 Hillwood Dr, Suite 160, Las Vegas, NV 89134, USA
[c] Department of Systems Engineering and Management, Air Force Institute of Technology, 2950 Hobson Way, WPAFB OH, 45433, USA

ARTICLE INFO

This manuscript was handled by Corrado Corradini, Editor-in-Chief, with the assistance of Patrick Lachassagne, Associate Editor

Keywords:
Analytical solution
Fate and transport
Parallel plate fracture-rock matrix
Poiseuille flow
Taylor dispersion

ABSTRACT

Modeling contaminant transport in fractured-rock matrix systems often approximates the effect of the parabolic flow field in the fractures (i.e., Poiseuille flow) on transport by adding a dispersion term to the uniform flow field. In this study, an analytical solution is derived to model contaminant transport in a parallel-plate fractured-rock matrix that explicitly simulates Poiseuille flow in the fractures, eliminating the need for the dispersion approximation. In addition to simulating Poiseuille flow in the fracture, the contaminant transport model developed here includes: (1) two-dimensional contaminant diffusion in the fractures and matrix, (2) first-order decay in the aqueous phase, and (3) rate-limited sorption onto matrix solids. It should be noted, however, that this model, much like the commonly employed Taylor dispersion approximation, neglects macro dispersion, thereby limiting the model's applicability to systems having wide fracture apertures with extremely high flow velocities ($P_e > 10^4$). Model equations are analytically solved in the Laplace domain and numerically inverted. In addition, analytical expressions for the zeroth, first, and second spatial moments of the concentration profiles along the fractures are derived for both the new Poiseuille flow model as well as a model that approximates the effect of Poiseuille flow on transport by using a dispersion term. The first and second moment expressions are used to quantify how well the dispersion term approximates the effect of Poiseuille flow. Simulations confirm that the dispersion approximation will be adequate for natural fractures at long times. However, if a modeler is concerned with short-time transport behavior or transport behavior in systems with relatively wide-aperture fractures and high groundwater velocities where macro dispersion can be ignored, such as may be found at engineered geothermal systems and carbon capture and storage sites, there may be significant differences between model simulations that explicitly incorporate Poiseuille flow and those that approximate Poiseuille flow with a dispersion term. The model presented here allows the modeler to analytically quantify these differences, which, depending on the modeling objective, may cause the dispersion approximation to be inadequate. Simulations were also run to examine the effect of adsorption rate on remediation of fractured-rock matrix systems. It was shown that moderate adsorption rate constants could lead to very long remediation times, if remediation success is quantified by achieving low concentrations within the fracture.

1. Introduction

Modeling fate and transport in fractured subsurface formations is of importance for investigating waste disposal, contaminant remediation and long-term environmental management of complex contaminated sites. There has been considerable effort devoted to characterizing and quantifying contaminant fate and transport in fractured-rock matrix systems (Berkowitz, 2002; Neretnieks, 2017; Li et al., 2020). Accidental release and waste disposal of hazardous chemicals have resulted in widespread subsurface contamination, often at locations where the subsurface includes a fractured-rock matrix, which makes remediation and site management even more challenging. The most concerning issues for environmental risk assessment and risk management at these complex contaminated sites are: (a) accurately quantifying the mechanisms governing contaminant fate and transport along the preferential fracture flow paths, and understanding the influence of retention in the rock matrix on this flow, (b) characterizing how a contaminant transported from a source zone will distribute in the fractured-rock matrix,

* Corresponding author.
E-mail address: huang.junqi@epa.gov (J. Huang).

https://doi.org/10.1016/j.jhydrol.2021.126097
Received 25 December 2020; Received in revised form 5 February 2021; Accepted 15 February 2021
Available online 20 February 2021
0022-1694/Published by Elsevier B.V.

and (c) describing the influence of the immobilized contaminant in the rock matrix on the evolution of the contaminant source zone. To reliably simulate the fate and transport of contaminants in such complex subsurface domains, mathematical models that accurately incorporate the important governing processes are needed.

Numerous models developed to simulate solute transport through a fractured-rock matrix have been proposed (e.g., Berkowitz, 2002; Neretnieks, 2017; Li et al., 2020). Among the most common is the single-fracture-path model. This model treats the fractured-rock matrix as a dual-domain medium consisting of fast flow zones, the fractures, and stagnant water zones, the rock matrix. Contaminant mass is transferred between the two zones. Typical solutions to single-fracture-path models can be found in Neretnieks (1980), Grisak and Pickens (1981), Tang et al. (1981), Sudicky and Frind (1982), Barker (1982), Chen (1986), Maloszewski and Zuber (1985, 1990), Roubinet et al. (2012), and Houseworth et al. (2013). Conventionally, the water velocity in a fracture is assumed to be uniform across the flow channel, while in the rock matrix, the stagnant water acts to store contaminant. The main processes affecting the movement of contaminants in such a system depicted in Fig. 1a are advection and dispersion in the fractures, sorption to the solid matrix, diffusion through the immobile matrix water and, in some cases, first-order biological or chemical decay.

While water flow in the single-fracture-path model is commonly assumed to be uniform, more realistically, the flow field is parabolic, with maximum velocity at the center of the fracture and zero velocity at the fracture wall, due to the no-slip condition (see Fig. 1b). This parabolic flow field is referred to as Poiseuille flow (Clark, 2009). To capture the contaminant spreading that results from Poiseuille flow in the fracture, a dispersion term (so-called Taylor dispersion (Taylor, 1953)) is introduced in the single-fracture-path, uniform flow model. This dispersion term attempts to approximate the spreading observed in the field by introducing an effective dispersion parameter. The value of the dispersion parameter (D_f) that simulates contaminant spreading at long times due to Poiseuille flow has been calculated as (Fischer et al., 1979; Detwiler et al., 2000; Wang et al., 2012; Liu et al., 2018): $D_f = D_m + 2(dv_a)^2/(105D_m)$, where D_m is the molecular diffusion coefficient; v_a is the average velocity in the fracture; and d is the half-aperture width of the fracture. Note that this approximation of the dispersion parameter (D_f) neglects macro dispersion (or geometrical dispersion), which is caused by velocity variations due to variations in the fracture aperture dimension (Roux et al., 1998; Detwiler et al., 2000; Boschan et al., 2008). Detwiler et al. (2000) demonstrate that Taylor dispersion dominates and macro dispersion may be neglected for values of the Peclet number ($Pe = 2v_a d/D_m$) greater than about 10^4.

In this paper we propose to couple Poiseuille flow in the fractures with diffusion in the rock matrix. Explicitly modeling the Poiseuille flow through the fracture eliminates the need to approximate spreading behavior using an artificial dispersion term approximation. While there has been extensive modeling of fractured-rock matrix systems (e.g., Berkowitz, 2002; Zhu et al., 2016; Neretnieks, 2017; Zhou et al., 2017; Zhu and Zhan, 2018; Chen and Zhan, 2018; Zhou and Zhan, 2018; Li et al., 2020) a thorough review of the literature found only a single

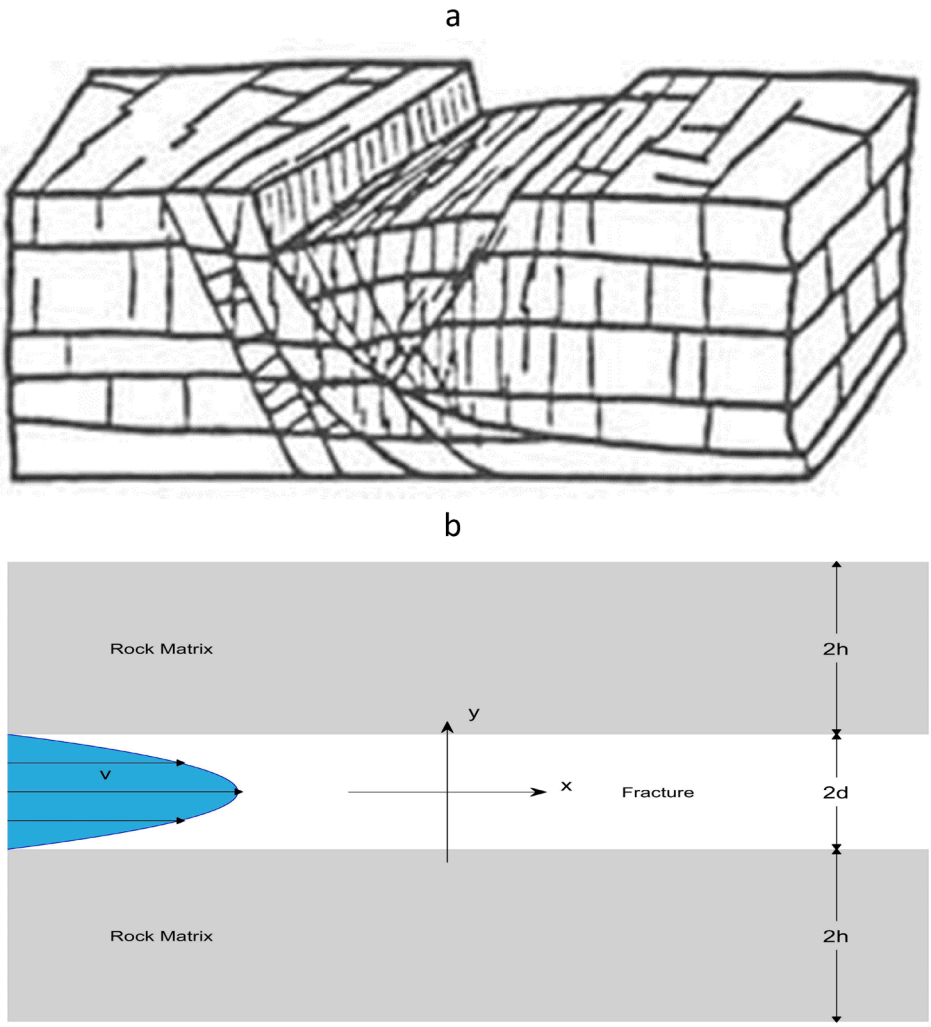

Fig. 1. (a) Conceptual model for fractured rock matrix (NRC, 1996) and (b) contaminant transport in single fracture-matrix model.

reference where Poiseuille flow was coupled with matrix diffusion (Bloechle, 2001). This model, however, is only applicable at late times and neglects the potential for contaminant degradation, which may have important impacts on contaminant fate and transport. Bloechle (2001) uses an asymptotic spectral comparison method (ASCM) to derive the approximate long-time solution to the model equations. Bloechle (2001) also derives the time-dependent behavior of the zeroth and first moments of the concentration distribution.

By contrast, this study derives an exact analytical solution in the Laplace domain to the model governing equations for Poiseuille flow in the fracture and diffusion in the rock matrix. The model equations also include terms describing first-order degradation in the aqueous phase and rate-limited sorption to matrix solids. The solution to the model equations in the Laplace domain is then numerically inverted to compute the contaminant concentration as a function of time. Analytical solutions to the spatial moments of the simulated concentration distributions along the fracture are also derived. The solutions presented here are applicable at all times. They can be used to more accurately and efficiently model contaminant fate and transport through fractured-rock matrix system that can be approximated as parallel plates, which will allow for the rapid evaluation of model parameters and their influence on contaminant fate and transport. This model can also be used to assess the error introduced by approximating spreading due to Poiseuille flow with a Taylor dispersion term, as the Taylor dispersion approximation is often employed out of mathematical convenience and has yet to be thoroughly evaluated to determine under what conditions the approximation may not apply. It is also important to note that both the parallel-plate Poiseuille model developed here, and the parallel-plate Taylor dispersion approximation commonly employed in the literature, neglect macro dispersion, which is an important process to incorporate when modeling fracture systems with P_e less than 10^4 (Detwiler et al., 2000). Finally, the analytical model presented here may be used to verify numerical modeling results.

2. Model description

A conceptual model of the fractured-rock matrix is depicted in Fig. 1b. The fractured-rock matrix is composed of identical slabs of rock matrix separated by equally spaced, planar fractures. This is commonly referred to as the single-path-fracture model. Solving this problem requires the following assumptions:

a) Water flow in the fractures is accurately described by Poiseuille's law, with a parabolic velocity distribution in the y-direction.
b) Contaminant transport in the fracture is governed by advection in the x-direction and molecular diffusion in the x- and y-directions.
c) Water in the rock matrix is immobile, with contaminant transport governed by diffusion in the x- and y-directions.
d) Mass transfer occurs at the interface between fractures and the rock matrix.
e) First-order decay may occur in the aqueous phase in both fracture and rock matrix zones.
f) Rate-limited adsorption occurs in the rock matrix zone.
g) The model depicted in Fig. 1b provides useful insights into contaminant transport in a rock-fracture matrix system, such as is depicted in Fig. 1a.
h) The two-dimensional representation of the rock-fracture matrix (x-y) is an accurate representation of behavior likely to occur in three dimensions. Therefore, macro dispersion, due to velocity variations in the plane of the fracture (Detwiler et al., 2000), is ignored.

Assumption (h) is perhaps the least realistic of the assumptions, as it requires either (1) a large value of *Pe* that would only be seen in very wide fractures with extremely high flow velocities, or (2) fracture widths that have very little variance. While this limits the applicability of the model to simulate natural systems, there are instances, as will be subsequently discussed in Section 6, where high *Pe* flow in fractures occurs, and consideration of Poiseuille flow is necessary.

3. Governing equations

Two-dimensional contaminant fate and transport in the fracture is governed by advection, molecular diffusion and first-order decay, which can be described by:

$$\frac{\partial C}{\partial t} = D_m\frac{\partial^2 C}{\partial x^2} - v(y)\frac{\partial C}{\partial x} + D_m\frac{\partial^2 C}{\partial y^2} - \lambda C \tag{1}$$

where C is the contaminant concentration in the liquid phase; $v(y)$ is the velocity of fluid varying in the y-direction within the fracture, D_m is the molecular diffusion coefficient; λ is the first-order degradation rate constant; t is time; x and y are spatial coordinates.

Poiseuille flow is described by a parabolic velocity profile in a fracture according to (Clark, 2009):

$$v(y) = \frac{3}{2}v_a\left(1 - \frac{y^2}{d^2}\right) \tag{2}$$

where, v_a is the average velocity in the fracture, and d is the half aperture of the fracture.

Transport in the rock matrix is described by the two-dimensional diffusion equation:

$$\theta\frac{\partial C_m}{\partial t} + \rho_b\frac{\partial S_m}{\partial t} = D_{ex}\frac{\partial^2 C_m}{\partial x^2} + D_{ey}\frac{\partial^2 C_m}{\partial y^2} - \theta\lambda_m C_m \tag{3}$$

where

$$\frac{\partial S_m}{\partial t} = \alpha(k_d C_m - S_m) \tag{4}$$

and C_m is the contaminant concentration in the liquid phase in the matrix; S_m is the contaminant concentration in the solid phase in the matrix; θ is the porosity of the rock matrix, ρ_b is the bulk density of the rock matrix, D_{ex} and D_{ey} are the effective diffusion coefficients in the x- and y-directions in the matrix, respectively, λ_m is the first-order degradation rate constant in the liquid phase in the matrix; α is the non-equilibrium adsorption rate constant; and k_d is the adsorption partitioning constant.

3.1. Initial conditions

To solve the set of governing equations given in (1) to (4), an initial condition that defines the distribution of contaminant along the fracture and in the matrix must be established. Although a variety of initial conditions can be set, the solution presented here assumed the following:

$$C = C_i(x), t = 0, -\infty < x < +\infty, 0 \le y \le b \tag{5a}$$

$$C_m = C_{mi}(x), t = 0, -\infty < x < +\infty, b \le y \le b + h \tag{5b}$$

$$S_m = k_d C_{mi}(x), t = 0, -\infty < x < +\infty, b \le y \le b + h \tag{5c}$$

where C_i and C_{mi} respectively are a function of x only, which implies the fracture and matrix are initially contaminated at concentrations that are invariant in the y direction. Equation (5c) indicates that the initial solid phase contaminant concentration in the matrix is in equilibrium with the dissolved phase matrix concentration.

3.2. Boundary conditions

The boundary conditions used to solve equations (1) to (4) establish the concentration at the fracture walls and at the middle of the rock matrix, as well as at the far extent of the fracture according to:

$$C = 0, x \to \pm\infty, 0 \le y \le b, t > 0 \tag{6a}$$

$$\frac{\partial C}{\partial y} = 0, y = 0, \ -\infty < x < \infty, t > 0 \tag{6b}$$

$$C = C_m, y = d, \ -\infty < x < \infty, t > 0 \tag{6c}$$

$$D_m \frac{\partial C}{\partial y} = D_{ey} \frac{\partial C_m}{\partial y}, y = d, \ -\infty < x < \infty, t > 0 \tag{6d}$$

$$C_m = 0, x \to \pm\infty, b \le y \le b + h, t > 0 \tag{6e}$$

$$\frac{\partial C_m}{\partial y} = 0, y = d + h, \ -\infty \le x \le \infty, t > 0 \tag{6f}$$

where, h is the half thickness of the rock matrix. Boundary condition (6b) indicates that no mass may pass through the center line of the fracture, implying a symmetric concentration distribution about the fracture center line. Boundary conditions (6c) and (6d) indicate the continuity of concentration and mass flux at the surface of the fracture walls, while (6f) indicates no mass may pass through the center line of the matrix – implying a symmetric concentration distribution in the matrix between adjacent fractures.

4. Model solutions

4.1. Poiseuille flow case

Having defined the governing equations, initial conditions and boundary conditions, the solution of equations (1), (3) and (4) can be developed using the Laplace transform in t and Fourier transform in x. Applying the initial conditions (5a to 5c), the Laplace transform of equations (1), (3) and (4) are:

$$D_m \frac{\partial^2 \overline{C}}{\partial x^2} - v(y) \frac{\partial \overline{C}}{\partial x} + D_m \frac{\partial^2 \overline{C}}{\partial y^2} - (p + \lambda)\overline{C} = -C_i(x) \tag{7}$$

$$D_{ex} \frac{\partial^2 \overline{C}_m}{\partial x^2} + D_{ey} \frac{\partial^2 \overline{C}_m}{\partial y^2} - f(p)\overline{C}_m = -g(p) C_{mi}(x) \tag{8}$$

$$f(p) = \theta(p + \lambda_m) + \frac{\alpha k_d \rho_b p}{p + \alpha} \tag{9a}$$

$$g(p) = \theta + \frac{\rho_b k_d \alpha}{p + \alpha} \tag{9b}$$

where the variables with overbar denote the Laplace transform and p is the Laplace transform variable.

Further, applying the Fourier transform to equations (7) and (8) subject to the boundary conditions (6a) and (6e), and substituting equation (2), results in equations transformed in both time and space:

$$\frac{\partial^2 \overline{C}}{\partial y^2} - \left(Ay^2 + B\right)\overline{C} = -\frac{1}{D_m} C_i(\xi) \tag{10}$$

$$\frac{\partial^2 \overline{C}_m}{\partial y^2} - E\overline{C}_m = -\frac{1}{D_{ey}} g C_{mi} \tag{11}$$

where

$$A(\xi) = -\frac{3 v_a}{2 d^2 D_m} \xi i \tag{12a}$$

$$B(\xi, p) = \frac{1}{D_m}(p + \lambda + \frac{3}{2} v_a \xi i) + \xi^2 \tag{12b}$$

$$E(\xi, p) = \frac{1}{D_{ey}}[f(p) + D_{ex}\xi^2] \tag{12c}$$

and the variables with the tilde denote the Fourier transform, and ξ is the Fourier transform variable.

Applying the boundary conditions (6c) and (6f), the solution of equation (11) is:

$$\overline{C}_m(\xi, y, p) = [\overline{C}\ (\xi, d, p) - \frac{1}{ED_{ey}} g C_{mi}] \ \frac{\cosh[\gamma_m(d + h - y)]}{\cosh(\gamma_m h)} + \frac{1}{ED_{ey}} g C_{mi} \tag{13}$$

where:

$$\gamma_m = \sqrt{E} \tag{14}$$

Substituting Eq. (13) into (6d) results in:

$$\frac{\partial \overline{C}}{\partial y} + \beta_m \overline{C} = \frac{\beta_m}{ED_{ey}} g C_{mi}, y = d \tag{15}$$

where:

$$\beta_m = \frac{D_{ey}}{D_m} \gamma_m tanh(\gamma_m h) \tag{16}$$

Note that Eq. (15) ensured continuity at the fracture-matrix boundary, which results in a third type boundary condition that can be used to solve the system of equations.

Using variable substitution [Polyanin and Zaitsev, 1995],

$$\overline{C} = e^{-z/2} w(z) \tag{17}$$

$$z = \sqrt{A} y^2 \tag{18}$$

the homogeneous counterpart of Eq. (10) becomes:

$$z \frac{\partial^2 w}{\partial z^2} + (b - z) \frac{\partial w}{\partial z} - aw = 0 \tag{19}$$

where:

$$a = \frac{1}{4}(\frac{B}{\sqrt{A}} + 1) \tag{20a}$$

$$b = \frac{1}{2} \tag{20b}$$

Eq. (19) is the confluent hypergeometric equation and has a pair of linearly independent solutions, $M(a, b, z)$ and $z^{1-b}M(1 + a - b, 2 - b, z)$, where $M(a, b, z)$ is the first kind of confluent hypergeometric function (Abramowitz and Stegun, 1970). Back substituting w through (17), we have the general solution of the non-homogeneous transformed Eq. (10):

$$\overline{C} = \Delta_1 e^{-\frac{z}{2}} M(a, b, z) + \Delta_2 e^{-\frac{z}{2}} z^{1-b} M(1 + a - b, 2 - b, z) + \overset{*}{\overline{C}}\ (\xi, y, p) \tag{21}$$

where, Δ_1 and Δ_2 are the integration constants and $\overline{C}^{\,*}(\xi, y, p)$ is the particular solution of the non-homogeneous equation (10). The particular solution may be solved using the Green's function method.

$$\overset{*}{\overline{C}}\ (\xi, y, p) = F_0[e^{-\frac{z}{2}} z^{1-b} M(1 + a - b, 2 - b, z) \int_0^y e^{-\frac{z}{2}} M(a, b, z) dy +$$

$$e^{-z/2} M(a, b, z) \int_y^d e^{-\frac{z}{2}} z^{1-b} M(1 + a - b, 2 - b, z) dy] \tag{22}$$

where:

$$F_0(\xi, p) = -\frac{1}{D_m \mathrm{A}^{1/4}} C_i(\xi) \tag{23}$$

and Δ_1 and Δ_2 are specified using the boundary conditions (6b) and (15). The application of these conditions leads to $\Delta_2 = 0$ and

$$\Delta_1(\xi, p) = \frac{\Phi_N}{\Phi_D} \frac{dw_1}{D_m} C_i + \frac{exp(z_d/2)}{\Phi_D} \frac{d\beta_m}{D_{ey} E} g C_{mi} \tag{24}$$

$$\Phi_N(\xi,p) = (\beta_m d + 1 - z_d)M(1+a-b,2-b,z_d) + 2z_d M^{'}(1+a-b,2-b,z_d) \tag{25a}$$

$$\Phi_D = (\beta_m d - z_d)M(a,b,z_d) + 2z_d M^{'}(a,b,z_d) \tag{25b}$$

$$w_1(\xi,p) = \int_0^d e^{-z/2}M(a,b,z)dy \tag{25c}$$

$$z_d = \sqrt{A}d^2 \tag{25d}$$

Substituting equations (22) and (24) into equation (21), allows for the solution to be written in the Laplace and Fourier domains as:

$$\overline{C}\ (\xi,y,p) = \Delta_1(\xi,p)e^{-z/2}M(a,b,z) + \overset{*}{\overline{C}}\ (\xi,y,p) \tag{26}$$

Applying the inverse Fourier transform, we obtain the solution in the Laplace domain:

$$\overline{C}(x,y,p) = \frac{1}{2\pi}\int_{-\infty}^{\infty}[\Delta_1(\xi,p)e^{-z/2}M(a,b,z) + \overset{*}{\overline{C}}\ (\xi,y,p)]e^{ix\xi}d\xi \tag{27}$$

Equation (27) is an analytical solution to the governing equations in the Laplace domain. This equation can be used to model the effect of Poiseuille flow in the fracture on contaminant transport without employing the Taylor dispersion coefficient as an effective parameter.

4.2. Mean concentration

To quantify the mean concentration across the fracture aperture, equation (27) may be integrated according to:

$$\overline{C}(x,p) = \frac{1}{d}\int_0^d \overline{C}(x,y,p)dy \tag{28}$$

Evaluation of Equation (28) is straightforward, which gives a solution to the1-D transport problem in the fracture. The distribution and breakthrough of this mean concentration characterizes the typical non-Fickian diffusion behavior that is observed due to the effects of Poiseuille flow coupled with mass transfer to the rock matrix.

4.3. Taylor dispersion case

Conventionally, Taylor dispersion is implemented to approximate the effect of Poiseuille flow in the fracture on contaminant transport. Coupled with a uniform velocity flow field in the x-direction, the Taylor dispersion coefficient accounts for the long-time impact on transport of the more realistic parabolic velocity flow field and molecular contaminant diffusion in the x- and y- directions. The Taylor model results in **a**n equivalent governing equation for transport in the fracture:

$$\frac{\partial C}{\partial t} = D_f\frac{\partial^2 C}{\partial x^2} - v_a\frac{\partial C}{\partial x} - \lambda C - \frac{1}{d}J_m \tag{29}$$

where, D_f is the Taylor dispersion coefficient represented as

$$D_f = D_m + \frac{2(dv_a)^2}{105D_m} \tag{30a}$$

and J_m is the mass flux of contaminant on the fracture wall, represented as

$$J_m = -D_{ey}\frac{\partial C_m}{\partial y}, y = d \tag{30b}$$

In the Laplace and Fourier domain, (30b) becomes:

$$\underset{m}{\overline{J}} = -D_{ey}\frac{\partial \overline{C}_m}{\partial y}, y = d \tag{30c}$$

Using equation (13), we have:

$$\underset{m}{\overline{J}}\ (\xi,p) = D_{ey}\gamma_m\left[\overline{C}\ (\xi,p) - \frac{1}{ED_{ey}}gC_{mi}\right]\tanh(\gamma_m h) \tag{30d}$$

Sequentially, equation (29) subject to initial condition (5a) and boundary condition (6a) can be solved to obtain a solution in the Laplace and Fourier domain:

$$\overline{C}\ (\xi,p) = \frac{1}{d(p+\lambda+v_a\xi i + D_f\xi^2) + D_m\beta_m}[dC_i(\xi) + \frac{D_m\beta_m}{ED_{ey}}g(p)C_{mi}(\xi)] \tag{31}$$

Applying the Fourier inverse transform yields:

$$\overline{C}(x,p) = \frac{1}{2\pi}\int_{-\infty}^{\infty}\frac{1}{d(p+\lambda+v_a\xi i+D_f\xi^2)+D_m\beta_m}\left[dC_i(\xi)+\frac{D_m\beta_m}{ED_{ey}}g(p)C_{mi}(\xi)\right]e^{i\xi x}d\xi \tag{32}$$

Equation (32), the solution of the Taylor dispersion model, can be compared directly to equation (28), the solution of the Poiseuille flow model, to quantify how the Taylor model approximation impacts concentration versus time and concentration versus space simulations.

4.4. Mass transfer and mass storage in the rock matrix

The solutions derived above can also be used to quantify the mass flux through the interface between the fracture and rock matrix. This mass flux is modeled according to:

$$F_{mas} = -D_{ey}\frac{\partial C_m}{\partial y}(x, y = d, t) \tag{33}$$

In the Laplace and Fourier domains, (33) has the form:

$$\underset{mas}{\overline{F}} = -D_{ey}\frac{\partial \overline{C}_m}{\partial y}(x, y = d, t) \tag{34}$$

Applying equation (13) and substituting equation (16), equation (34) can be re-written:

$$\underset{mas}{\overline{F}}\ (\xi,d,p) = D_m\beta_m[\overline{C}\ (\xi,d,p) - \frac{1}{ED_{ey}}gC_{mi}] \tag{35}$$

Since the Fourier transform of the mean concentration is represented as:

$$\overline{\overline{C}}\ (\xi,p) = \int_{-\infty}^{\infty}\overline{C}(x,p)e^{-\xi x}dx \tag{36}$$

The zero-order moment, i.e. setting $\xi = 0$, gives the total mass stored in the fracture at time t:

$$M_{tot} = \overline{\overline{C}}\ (0,p)d \tag{37}$$

Therefore, it is relatively straightforward to compute the total mass stored in the rock matrix as:

$$M_{tot}^m = M_{ini} - M_{tot} \tag{38}$$

where, M_{ini} is the total mass initially stored in the system.

5. Evaluation of model solutions

Model solutions are evaluated using the baseline parameter values listed in Table 1. Two initial concentration distributions are proposed, a constant slug and a Dirac pulse.

5.1. Solution verification for an initial constant concentration slug distribution

A constant concentration slug is assumed to reside in a finite region:

$$C_i(x) = C_0[H(x-x_a) - H(x-x_b)] \tag{39}$$

Table 1
Base line parameter values used for simulations.

Parameter	v_a (m/day)	d (m)	h (m)	D_m (m^2/day)	λ (1/day)	θ	ρ_b (kg/L)	α (1/day)	k_d (L/kg)
Value	3.0	7.5e−3	1.0e−2	1.3e−4	1e−4	0.4	1.67	3e−2	0.45
Parameter	D_{ex} (m^2/day)	D_{ey} (m^2/day)	λ_m (1/day)	D_f (m^2/day)	C_0 (mg/L)	C_{m0} (mg/L)	M_0 (g/m)	x_a (m)	x_b (m)
Value	6.5e−5	6.5e−5	2e−5	0.0743	420	420	75	−10	10

where, C_0 is a constant, $H(x)$ is the Heaviside step function, x_a and x_b are spatial locations that bound the concentration distribution ($x_a < x_b$). In the Fourier domain (39) becomes:

$$C_i(\xi) = C_0 \frac{e^{-ix_a\xi} - e^{-ix_b\xi}}{i\xi} \tag{40}$$

Though the analytical solutions are somewhat complex, the numerical evaluation is readily implementable. The Laplace domain solutions given in Eqs. (27) and (28) are numerically inverted using the inversion method presented by de Hoog et al. (1982) as implemented in MATLAB by Hollenbeck (1998). The solution includes a special function, i.e. the confluent hypergeometric function, which is calculated using Algorithm 707, a Fortran subroutine collected from ACM (Nardin et al., 1992). The solution also includes calculus associated with the confluent hypergeometric function, for which some extensive numerical evaluations are needed. For confirming the correctness of the analytical solution, which relies on numerical Laplace inversion and evaluations of various functions, an alternative algorithm is used to compare with the analytical solution. The algorithm, designed as a semi-numerical method, numerically solves the intermediate equation (10) subject to the boundary conditions (6b) and (15) using a finite-difference method. The analytical and semi-numerical solutions are compared in Fig. 2a and 2b, where the concentration breakthroughs at three observation locations and the concentration spatial profile along the fracture at three times are respectively depicted. Both the analytical and semi-numerical solutions are in excellent agreement; giving confidence in the correctness of the analytical solution. Note that in Fig. 2, as well as in subsequent figures, the value of the concentration simulated by the Poiseuille flow model at a given value of x is the mean of the concentrations in the fracture transverse to the flow direction, since concentration varies within the fracture at position x as a function of y.

Fig. 2 also shows the expected contaminant transport behavior in a fractured-rock matrix; a sharp breakthrough as the front makes its way through the fracture, followed by long tailing as contaminant sequestered in the matrix slowly diffuses back into the fracture.

5.2. Sensitivity to fracture aperture and matrix thickness

In Fig. 3, the concentration breakthrough curves at three observation locations are depicted for three fracture aperture half-widths (d). Simulations are run for both the Poiseuille flow model and the model that uses Taylor dispersion to approximate the effect of Poiseuille flow on transport. It may be seen that the use of the Taylor dispersion approximation introduces very little error and the approximation improves at greater times. The figure shows that when the fracture aperture is relatively large, e.g., $d = 10.0$ mm, breakthrough arrives quickly and has a small tail, indicating less mass contribution from the rock-matrix; while for smaller fracture aperture widths, breakthrough is slowed, spreading is enhanced, and tailing is more significant. This is a consequence of the rock-matrix exerting a more significant influence on transport, resulting in more retardation, spreading, and enhanced tailing.

Rock-matrix half-thickness (h) is another parameter that is expected to influence transport, as it controls the buffer capacity (i.e., storage) of

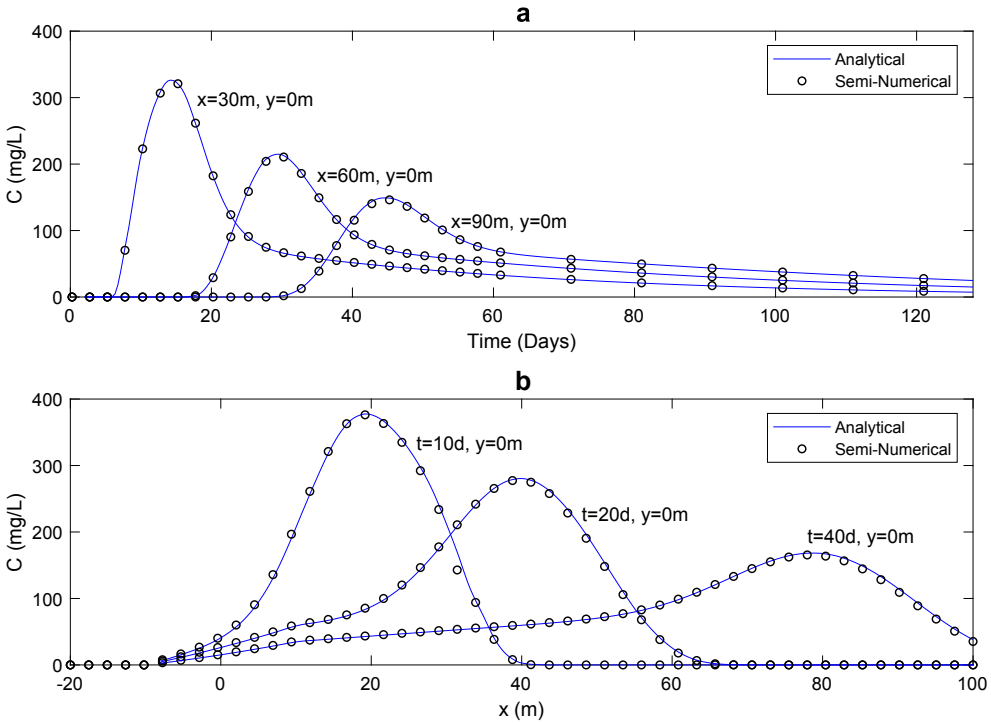

Fig. 2. Concentration (a) breakthrough curves at three down gradient observation points and (b) concentration spatial profile along the fracture at three selected times comparing the complete analytical solution and the semi-numerical solution using model parameters listed in Table 1.

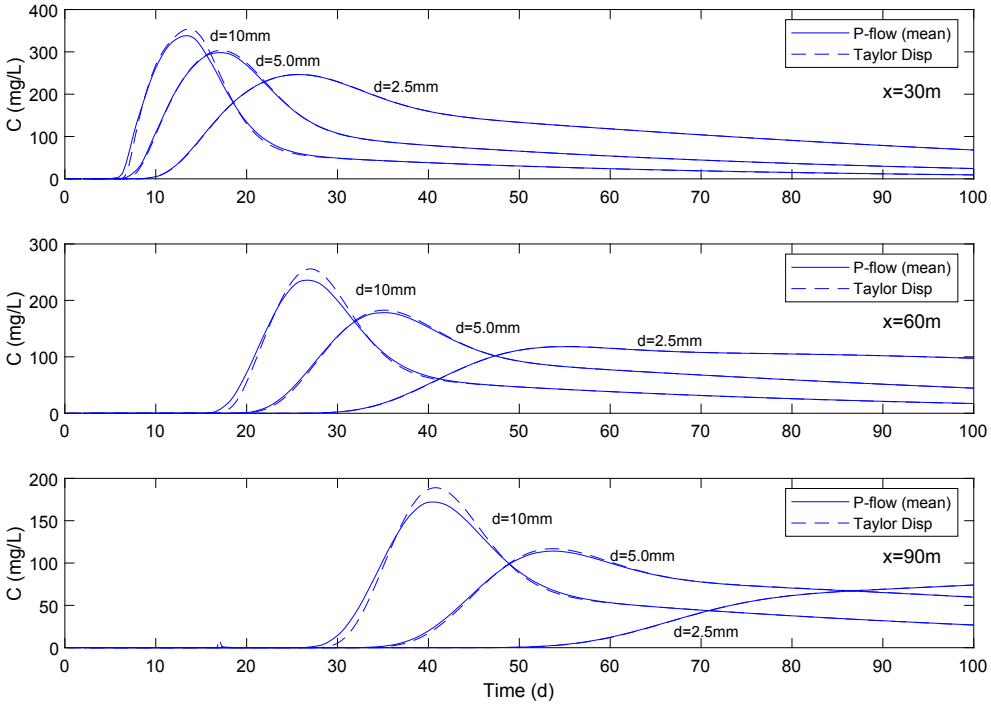

Fig. 3. Concentration breakthrough curves at three locations, comparing the Poiseuille Flow (P-flow) and Taylor dispersion models for three fracture aperture half-widths using model parameters listed in Table 1.

the system. The concentration breakthroughs at three locations are depicted in Fig. 4 for three rock-matrix half-thickness values. Breakthrough simulations shown in Fig. 4 are for both the Poiseuille flow model and the model that uses Taylor dispersion to approximate the effect of Poiseuille flow on transport. Again the use of the Taylor dispersion approximation introduces very little error. A narrow and high concentration peak corresponds to a smaller$h$; while smoother concentration peaks with increasing retardation, spreading, and tailing occur for larger h, which shows that as the influence of the rock-matrix on transport increases, retardation, spreading, and tailing increase.

5.3. Dirac pulse initial condition

An instantaneous mass M_0 input into a fracture at $x = x_0$ may be

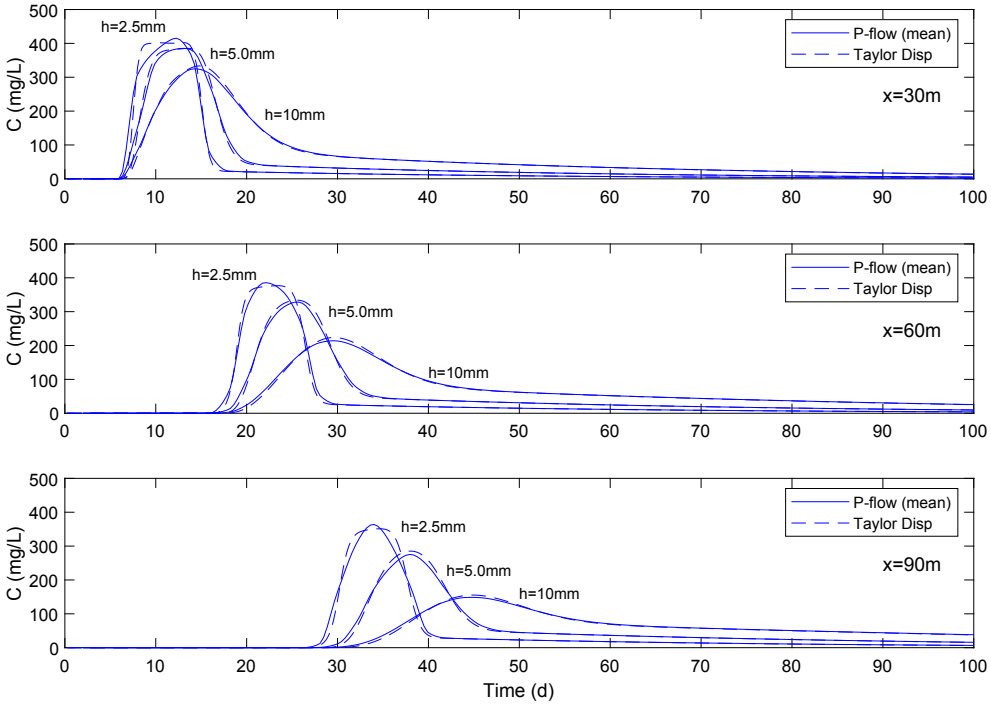

Fig. 4. Concentration breakthrough curves at three locations, comparing the Poiseuille Flow (P-flow) and Taylor dispersion models for three rock-matrix half-thicknesses using model parameters listed in Table 1.

modeled using a Dirac pulse function:

$$C_i(x) = \frac{1}{2d} M_0 \delta(x - x_0) \tag{47}$$

where, $\delta(x)$ is the Dirac delta function. In the Fourier domain:

$$C_i(\xi) = \frac{1}{2d} M_0 e^{-ix_0\xi} \tag{48}$$

Fig. 5(a) depicts the concentration breakthrough at three locations, and Fig. 5(b) shows the concentration profile along the fracture at three times for an instantaneous input of $M_0 = 75\mathrm{g}/m$, which corresponds to an initial concentration (C_0) of 5000 mg/L in a fracture of width $2d = 15 \times 10^{-3} m$. The characteristics of the contaminant breakthrough curve and the contaminant distribution in space are consistent with the expectation of an initial sharp breakthrough with tailing, eventually becoming more symmetric over time.

5.4. Effect of different initial contamination scenarios

Fig. 6a and 6b show the breakthrough curves and concentration spatial profiles along the fracture, respectively, for three scenarios: (1) an initially contaminated fracture and matrix, (2) an initially contaminated fracture, but clean matrix, and (3) an initially contaminated matrix, and clean fracture. In the latter two scenarios it's important to note that boundary condition (6C) is only applicable for t > 0. As described in Table 1, the initial contaminated zone exists between $-10 \leq x \leq 10$; $|x| > 10$ is initially clean. In Fig. 6a we see that the initial breakthrough for the initially contaminated matrix, clean fracture scenario slightly lags the two breakthrough curves where the fracture is initially contaminated. This is a consequence of the time it takes for the contamination in the matrix to diffuse into the fracture before being advected to the sampling locations. We also see that as would be expected, the breakthrough curves for the two scenarios that include initial contamination in the matrix have more significant tailing than the breakthrough curve where the matrix is initially uncontaminated, though importantly, all three breakthrough curves exhibit tailing, due to diffusion into the matrix from the fracture, with subsequent back diffusion. We may notice that the areas under the three breakthrough curves (i.e., the curves' zeroth moments) are different. Area under the breakthrough curve is proportional to mass of contaminant passing the sampling point, and since each of the three scenarios has a different initial mass of contamination, the areas and corresponding zeroth moments should be different.

Fig. 6b shows the concentration spatial profile in the fracture for each of the above three scenarios. We see that after three days, the front for the scenario where the matrix is initially contaminated, but the fracture is clean lags the two fronts where the fracture is initially contaminated. This observation is consistent with the rapid transport of contaminant within the fracture. After 30 days, the concentration profiles for the two scenarios that include contaminant in the matrix initially have more significant tailing than the uncontaminated matrix scenario. This reflects the additional contamination in the system and the extended time for the contaminant to diffuse from the rock matrix. Though it is worth noting that the 30-day concentration peaks are all approximately the same and all three distributions exhibit significant tailing, since even for the scenario where there was no initial contaminant in the matrix, subsequent diffusion from the fracture into the matrix results in tailing.

To examine the effect of adsorption on remediation of an initially contaminated system, another set of simulations was run using the scenario where contaminant is initially distributed in both the fracture and rock matrix. Fig. 7 examines the impact of the non-equilibrium adsorption rate constant (α) on the breakthrough (Fig. 7a) and concentration spatial profile (Fig. 7b) curves. The figure shows that at large ($\alpha = 3 \times 10^{-1} d^{-1}$) and small ($\alpha = 3 \times 10^{-4} d^{-1}$) adsorption rates (compared to the rates of the other transport processes like advection), both the breakthrough curves and concentration spatial profiles are relatively symmetric, while there is significant asymmetry and tailing at moderate $\left(\alpha = 3 \times 10^{-2} d^{-1}\right)$ adsorption rates. This behavior is characteristic of scenarios that involve remediation of systems where adsorption to solids is rate limited (Goltz and Oxley, 1991; Goltz and Huang, 2017). At very high adsorption rates, adsorption approaches equilibrium, where breakthrough and spatial profiles are symmetric and retarded. At very low adsorption rates, adsorption has minimal impact

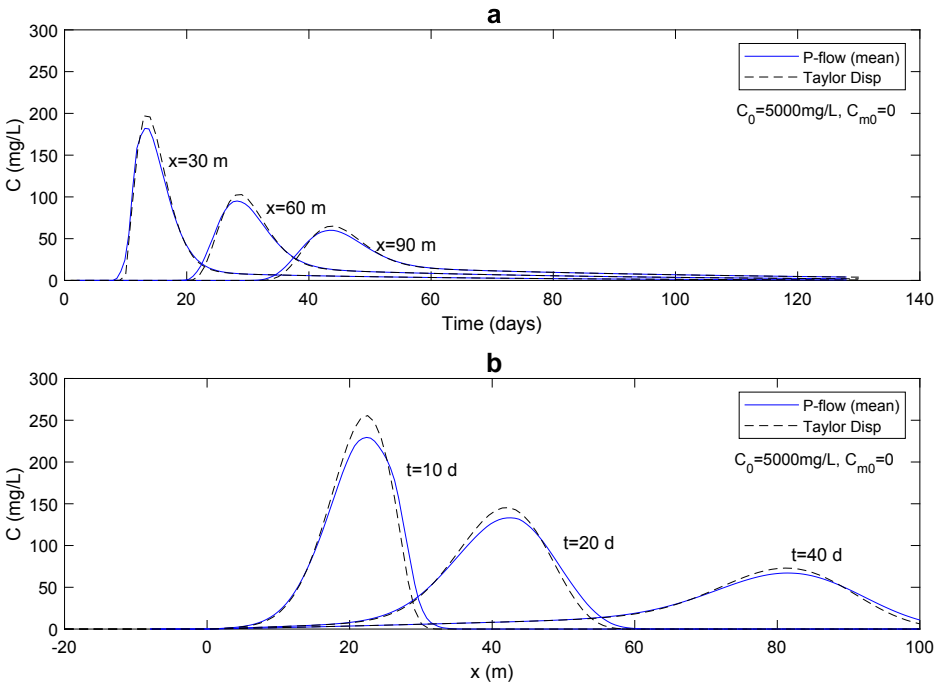

Fig. 5. Concentration (a) breakthrough at three locations and (b) concentration spatial profile along the fracture at three times for an initial mass released at $x = 0$, using the model parameters listed in Table 1.

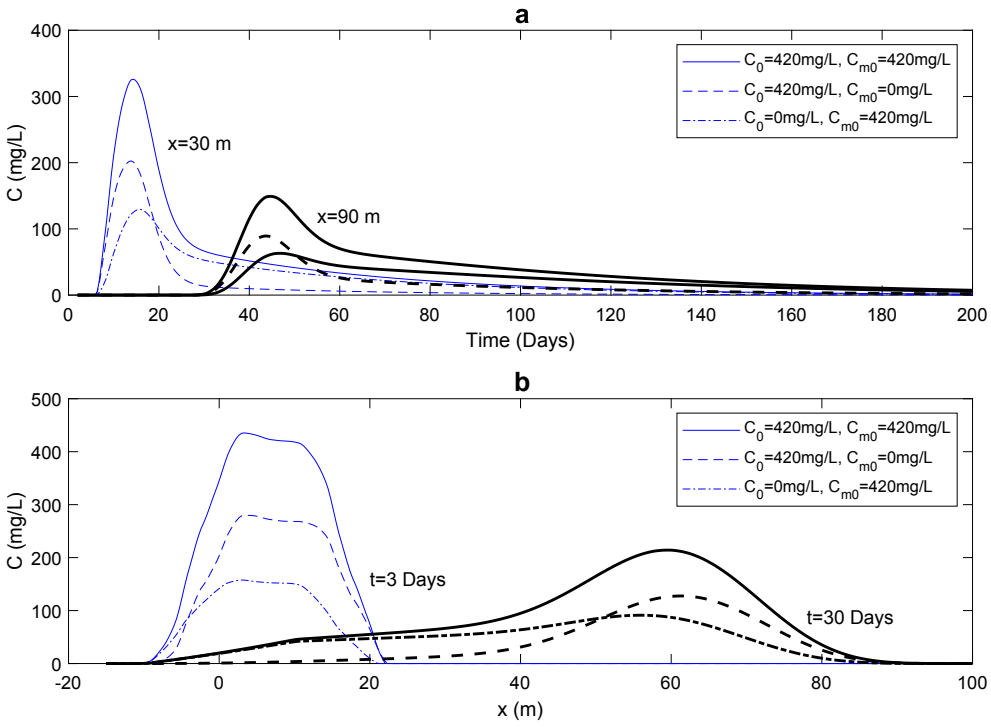

Fig. 6. (a) Concentration breakthrough curves and (b) concentration spatial profiles along the fracture for three scenarios: (1) initially contaminated fracture and matrix, (2) initially contaminated fracture, clean matrix, and (3) initially contaminated matrix, clean fracture using the model parameters listed in Table 1.

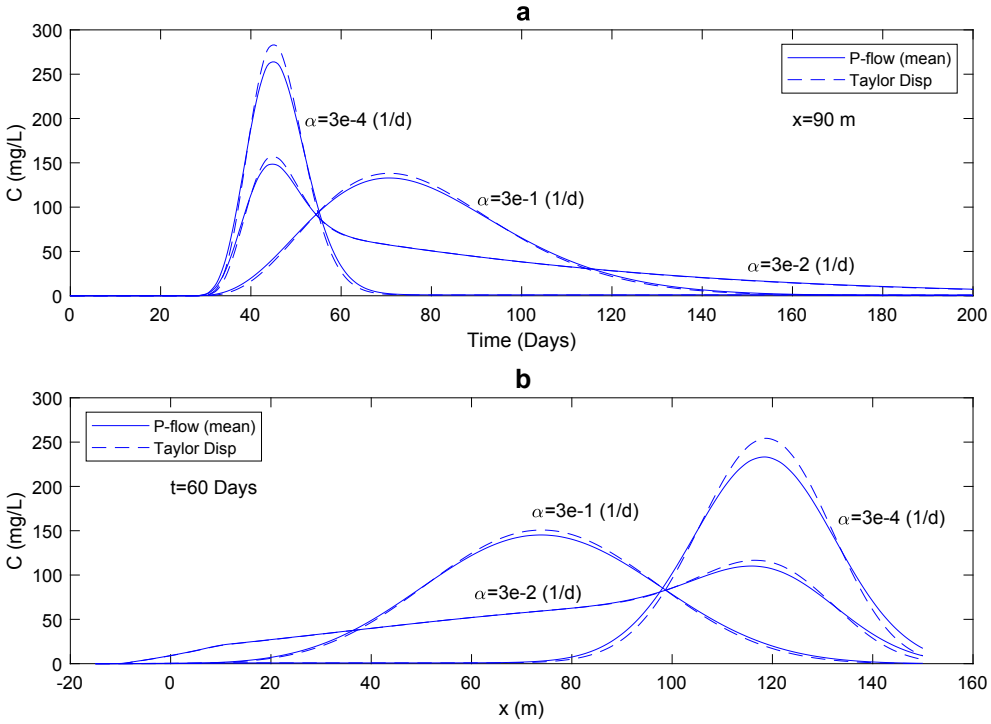

Fig. 7. (a) Concentration breakthrough at $x = 90$ m and (b) concentration spatial profile along the fracture after 60 days, for various values of the adsorption rate constant (α). The data calculated from the Taylor dispersion model are also displayed for confirmations and comparisons.

on transport, so the simulations only reflect the effects of advection and dispersion, thereby resulting in relatively symmetric breakthrough and spatial profiles. It is only at moderate rates, that is when the adsorption rate is comparable to the rates of the other transport processes like advection, does one see the early breakthrough and tailing characteristic of transport when adsorption is rate limited. This significantly impacts remediation, as the time to achieve a specified concentration level of contaminant when adsorption rates are moderate may be orders of magnitude greater than when adsorption is either fast or slow (Goltz and Oxley, 1991; Goltz and Huang, 2017). Fig. 7 also shows that the Taylor dispersion approximation does a reasonable job of approximating Poiseuille flow with only a slight over-prediction of the peak

concentrations.

Given that non-equilibrium (i.e., rate-limited) sorption may occur in the rock matrix, it's important to examine the impact on mass sequestered. Fig. 8 depicts the mass sequestered in the fracture and rock matrix as a function of time for four different non-equilibrium sorption rate constants (α = 0.0, 0.0003, 0.03, and 0.3 d^{-1}) and two different initial conditions – one where the initial mass is only in the fracture (Fig. 8a) and one where the initial mass is only in the matrix (Fig. 8b). When α = 0.0 d^{-1} there is no mass sorbed to the rock matrix solids, indicating that k_d also is equal to 0.0 L/kg. Degradation is assumed to be negligible ($\lambda = 0d^{-1}$).

Fig. 8a and 8b exhibit the same behavior, only in opposite directions, with mass being transferred from the fracture to the rock matrix in Fig. 8a and mass being transferred from the rock matrix to the fracture in Fig. 8b. The rate at which mass moves is a function of the adsorption rate constant, α. As the value of α increases from 0.0003 d^{-1} to 0.03 d^{-1} to 0.3 d^{-1}, the time for the system to reach equilibrium decreases, from approximately 10^4 d to 10^2 d to 10 d, respectively, since the rate of desorption of mass from the rock matrix solids increases as the value of α increases. When α = 0.0 d^{-1}, as indicated by the solid lines in Fig. 8, equilibration is fast since there is no mass sorbed onto the rock matrix solids. In this case, the time to equilibration only depends on the rate at which mass is transferred in the liquid phase between the fracture and rock matrix (i.e., diffusion into/out of the rock matrix). When the system achieves equilibrium at long times, the figure shows that the ratio of mass stored in the rock matrix (dissolved plus sorbed mass) to the dissolved mass stored in the fracture is:

$$\frac{Massinrock}{Massinfracture} = \frac{C_m \cdot 2h\theta \int_{-\infty}^{\infty} dx + \rho_b k_d C_m \cdot 2h \int_{-\infty}^{\infty} dx}{C \cdot 2d \int_{-\infty}^{\infty} dx} = \frac{h\theta + \rho_b k_d h}{d} \quad (49)$$

since at equilibrium $C = C_m$. For the Table 1 parameter values the ratio is 1.54. When α = 0.0 d^{-1}, which also means k_d = 0.0 L/kg, the ratio is 0.53. Of course, since there's no degradation, the total mass in the system remains constant throughout time. The plots also show an interesting characteristic of the mass vs time profile which is evident when the adsorption rate constant is very low; see the dashed lines for the α = 0.0003 d^{-1} scenario. After an initial period of about 2 days, when mass is transferred relatively rapidly due to the concentration gradient in the liquid phase between the rock matrix and the fracture, mass transfer remains extremely slow so that it is only after 10^4 days that equilibrium is ultimately achieved. This slow rate of mass transfer is due to the very slow rate of desorption from the rock matrix solids. Taking account of the log-scale on the x-axis, we see that the rate of mass transfer between the fracture and rock matrix is relatively constant over time; on the order of several grams per thousand days. This mass behavior corresponds to the long but unseen tail for the α = 0.0003 d^{-1} simulated breakthrough curve shown in Fig. 7a, where undetectably low concentrations of contaminant leach out from the rock matrix to the fracture over decades.

Fig. 9a and b show similar mass transfer behavior. However, because there is degradation contaminant mass ultimately goes to zero in both the rock matrix and fracture. Note that the time to achieve zero mass, approximately 10^5 d, is the same, regardless of the value of the adsorption rate constant. The time is a function of the value of the degradation rate constant, λ.

6. Analysis of the adequacy of the Taylor dispersion approximation

Although the Taylor dispersion approximation was shown to give relatively accurate predictions in some scenarios depicted in section 4, the model developed here can be used to examine those conditions under which the Taylor dispersion scenario is no longer accurate. To perform this evaluation we derive analytical solutions for the zeroth, first, and second spatial moments of the Poiseuille flow and Taylor dispersion models (see Appendices A and B). The zeroth moment is a measure of the dissolved contaminant mass in the fracture at the sampling time, the first moment quantifies the displacement of the dissolved contaminant mass peak along the fracture at a given sampling time, and the second moment quantifies the spread of the dissolved contaminant

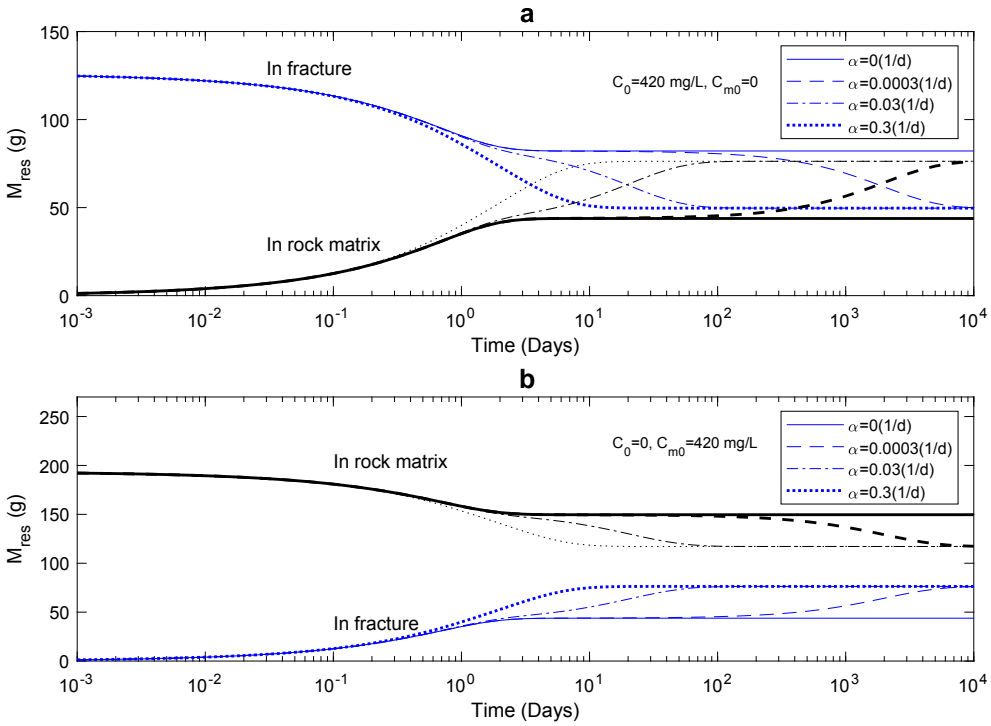

Fig. 8. Residual mass in the fracture and rock matrix versus time for Table 1 parameter values but with no degradation (λ = 0) at various values of the adsorption rate constant (α) for two scenarios: (a) initial contamination only in the fracture and (b) initial contamination only in the rock matrix. Masses are calculated for a three-dimensional system, assuming a 1 m cross-section.

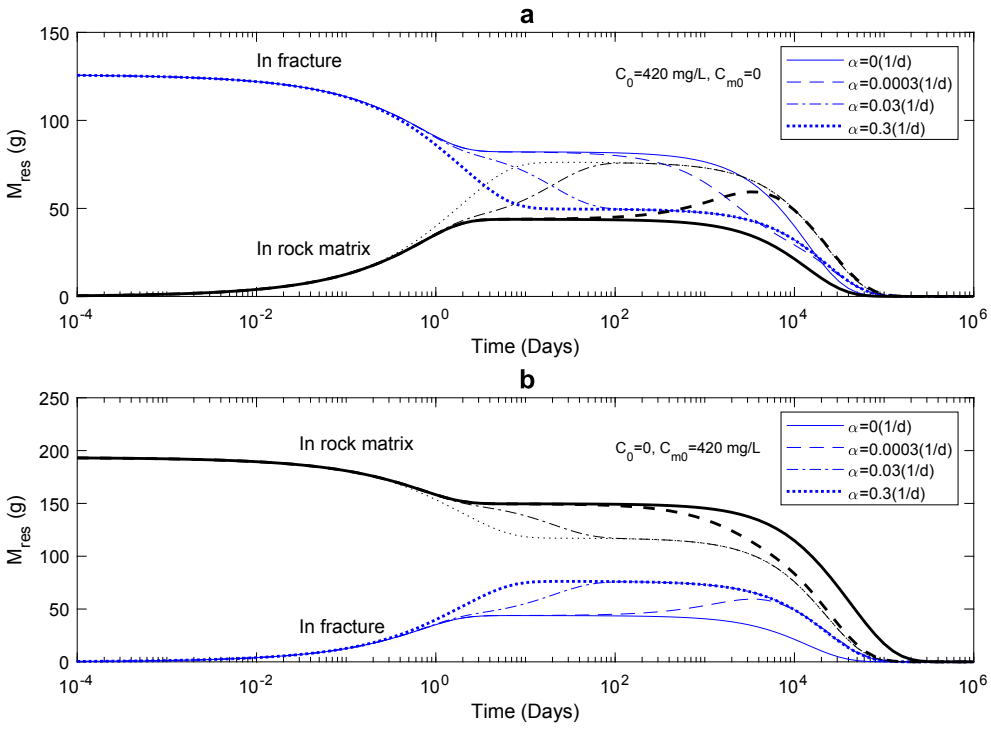

Fig. 9. Residual mass in the fracture and rock matrix versus time for Table 1 parameter values (including $\lambda = 1.0 \times 10^{-4}$ d^{-1}) at various values of the adsorption rate constant (α) for two scenarios: (a) initial contamination only in the fracture and (b) initial contamination only in the rock matrix. Masses are calculated for a three-dimensional system, assuming a 1 m cross-section.

mass around the peak.

In particular, the difference between the two models' simulations of the first and second moments may be used to quantify how well Taylor dispersion approximates the effect of Poiseuille flow on transport. Figs. 10 and 11 plot the relative difference in the spatial first and second moments respectively simulated by each of the two models versus sampling time for various scenarios. The plots were constructed using the specific parameter values in Table 1 as a baseline; however, it is possible to make a number of generalizations based on the results. First, Figs. 10 and 11 show that in all cases, at long times, the Taylor

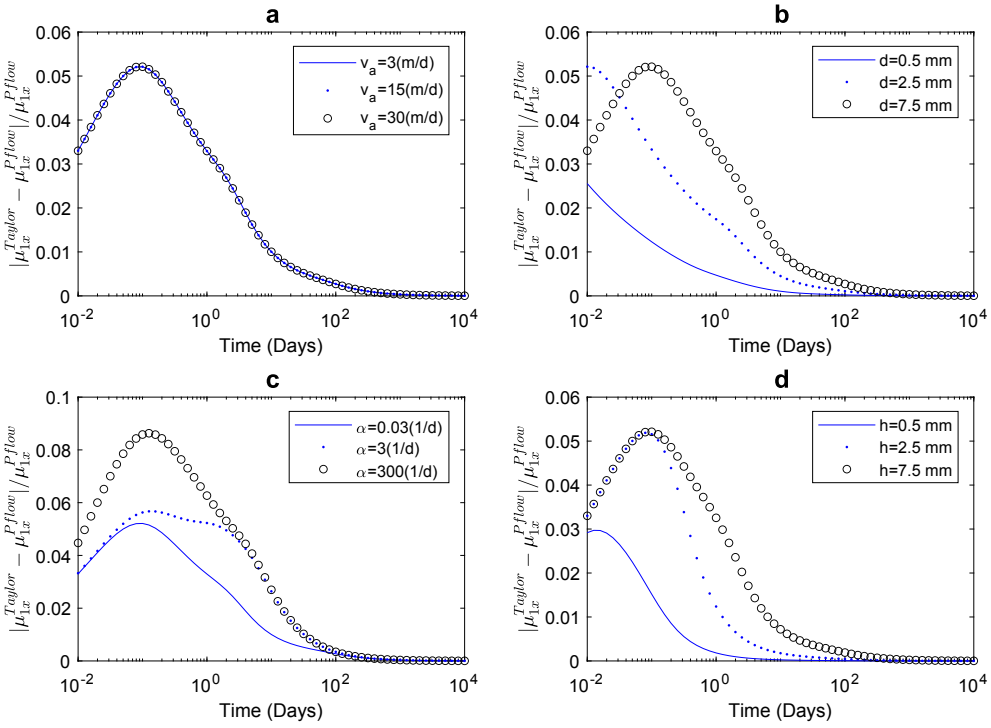

Fig. 10. Relative difference between first spatial moments calculated for the Poiseuille Flow and Taylor dispersion models over time for various values of (a) average velocity in the fracture (v_a), (b) half fracture aperture width (d), (c) adsorption rate constant (α), and (d) half matrix thickness (h). Model parameters listed in Table 1.

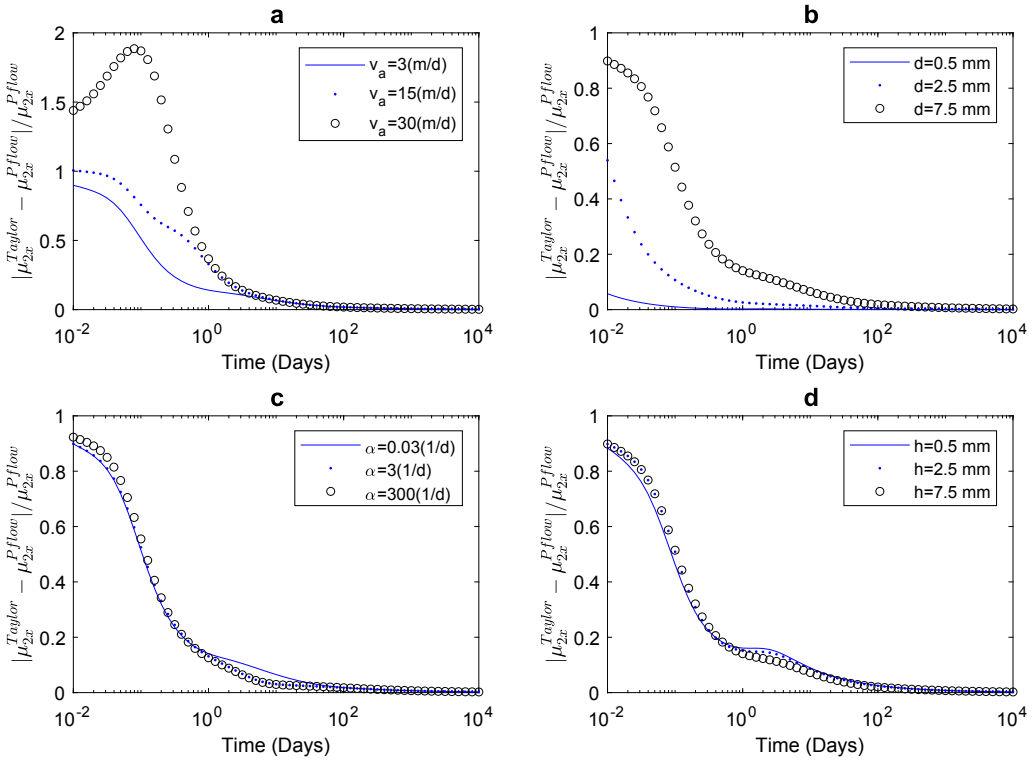

Fig. 11. Relative difference between second spatial moments calculated for the Poiseuille Flow and Taylor dispersion models over time for various values of (a) average velocity in the fracture (v_a), (b) half fracture aperture width (d), (c) adsorption rate constant (α), and (d) half matrix thickness (h). Model parameters listed in Table 1.

dispersion approximation model provides a reasonably accurate prediction of the Poiseuille flow model. It is only at relatively short times (less than about a day) that there is a significant difference between the modeled results. Relative differences in the first spatial moment are generally less than 10%. Relative differences in the second spatial moment, however, can be significant, often as much as a factor of 1 to 1.5 more than the spreading predicted by the Poiseuille flow model. However, even these differences decline with time to less than 20 percent within the first day.

From the figures, we also see that relative differences between the model predictions at early times are a maximum when: (1) the average velocity is high (Fig. 11a), (2) the fracture half-aperture width is large (Fig. 10b and 11b), (3) the adsorption rate is fast (Fig. 10c), and the half-thickness of the rock matrix is large (Fig. 10d). Fig. 11a demonstrates that as average velocity increases, the difference between the second moment predictions of the two models increases. This is expected, as the second moment is indicative of spreading (dispersion). We see from the second term on the right hand side of equation (30a) that the dispersion term used in the Taylor approximation increases as the square of the average velocity. Fig. 10b and 11b show the effect of the fracture half aperture width on the difference between the two models' simulations. As the fracture half aperture increases, the difference between the two models increases. This may be explained by the fact that for larger fracture apertures the velocity differences in Poiseuille flow are more pronounced, and the effects of diffusion within the fracture more significant. Thus, the Taylor approximation becomes less accurate as the fracture aperture increases. Fig. 10c and 10d demonstrate the effect of the adsorption rate constant and the rock matrix half thickness on the difference between the two models' simulations. The effects are similar for both the adsorption rate constant and the rock matrix half thickness. As the adsorption rate constant and the rock matrix half thickness increase, more mass may be sequestered in the rock matrix, thereby increasing the difference in the simulations of the two models. Comparing the y-axes of Figs. 10 and 11, we also see that the Taylor dispersion approximation has a much greater effect on the relative error of the second moment, which is related to spreading, rather than the first moment, which is related to displacement.

Hence, interpreting Figs. 10 and 11 illustrates that for natural fractures, which typically have aperture half-widths less than 0.5 mm (Vandersteen et al., 2003; Brabazon et al., 2019), and average velocities of less than 1 m/d (Schäfer et al., 2004), the Taylor approximation is adequate. However, the figures also show that under certain conditions there are significant differences between simulations of the Poiseuille flow model and a model that uses the Taylor approximation. As an example, Kittilä et al. (2020) conducted a tracer experiment at an engineered geothermal systems (EGS) site where hydraulic fracturing was used to improve injectivity. Fracture apertures on the order of 1–2 cm and flow velocities ranging from 10 to 220 m/d were inferred from the tracer data. Such conditions correspond to Peclet numbers as high as 4×10^4 where macro dispersion could be ignored, and in this scenario, depending on the modeling objective, these fracture characteristics may require consideration of Poiseuille flow as the Taylor approximation may provide a poor prediction of contaminant transport.

Thus, while the results in Figs. 10 and 11 show that under natural conditions the Taylor approximation adequately captures the important attributes of the Poiseuille flow model, there may be instances, particularly when fractures are artificially induced and flow is imposed, that the Poiseuille flow model is required to meet modeling objectives. In particular, large aperture fractures with high flow velocities may be seen in conjunction with carbon capture and storage (CCS) and EGS projects, which are increasingly being implemented throughout the globe. Fractures associated with EGS and CCS, which can be on the order of millimeters, may be the result of hydraulic fracturing that is undertaken to improve injectivity (Li, 2016). CCS projects may also see fracture width growth from exposure to carbon dioxide-acidified brine (Deng et al., 2013; Ellis et al., 2011).

7. Conclusions

Single fracture path models are useful for hypothesis testing and evaluation of groundwater cleanup in rock aquifers. The preceding analysis shows that in general, and especially at long times, the commonly used Taylor dispersion will, for most modeling needs, adequately approximate the effect on transport of Poiseuille flow in natural fractures. However, at short times the approximation may be inadequate, especially for artificially induced fractures that have relatively large (say $\geq$ 1.0 mm) fracture aperture half-widths and high groundwater velocities. In those cases, depending on the modeling objective, it may be appropriate to incorporate Poiseuille flow in the model. This paper presents an approach that allows the modeler to analytically quantify, for specified parameter values, how large a difference there will be between simulations of a model that explicitly incorporates Poiseuille flow and one that approximates Poiseuille flow with Taylor dispersion.

Model simulations also showed that for fractured-rock matrix systems that are characterized by moderate adsorption rate constants, remediation times could be extremely long, if remediation success is quantified by achieving low concentrations within the fracture.

CRediT authorship contribution statement

Junqi Huang: Conceptualization, Methodology, Visualization. **John Christ:** Writing - original draft, Writing - review & editing. **Mark N. Goltz:** Supervision, Validation, Writing - review & editing.

Declaration of Competing Interest

The authors declare that they have no known competing financial interests or personal relationships that could have appeared to influence the work reported in this paper.

Acknowledgments

The EPA through its Office of Research and Development funded and conducted this research. Portions of this research were supported by the Strategic Environmental Research and Development Program (SERDP), Project ER-1737. The views expressed in this paper are those of the authors and do not necessarily reflect the views or policies of EPA and DoD. Mention of trade names or commercial products does not constitute endorsement or recommendation for use. The authors wish to acknowledge and thank Dr. Jeff Yang and Dr. Stephen Kraemer of ORD, U.S. EPA for their review and commentary on this paper. The authors are grateful for the constructive comments from the Editor and two anonymous reviewers.

Research Data

Data in this paper were generated using the models and input parameters that were fully described in the text. The data generated for plotting all figures of this paper are available upon request by e-mail: huang.junqi@epa.gov.

Appendix A. Spatial moments of Poiseuille flow model

Equation (10), rewritten here for convenience is denoted in the Laplace and Fourier domains as:

$$\frac{\partial^2 \overline{C}}{\partial y^2} - \left(Ay^2 + B\right)\overline{C} = -\frac{1}{D_m} C_i(\xi) \tag{A.1}$$

Equation (A.1) is subject to the boundary conditions:

$$\frac{\partial \overline{C}}{\partial y} = 0, y = 0 \tag{A.2}$$

$$\frac{\partial \overline{C}}{\partial y} + \beta_m \overline{C} = \frac{\beta_m}{ED_{ey}} g C_{mi}, y = d \tag{A.3}$$

Zeroth spatial moment

Based on the definition of spatial moments, the zeroth spatial moment (m_{0x}) is calculated as

$$m_{0x} = \widetilde{\overline{C}}(\xi = 0, y, p) \tag{A.4}$$

where the zeroth spatial moment satisfies following governing equation (A.5) and boundary conditions (A.6, A.7):

$$\frac{\partial^2 m_{0x}}{\partial y^2} - B_0 m_{0x} = -\frac{1}{D_m} C_0(x_b - x_a) \tag{A.5}$$

$$\frac{\partial m_{0x}}{\partial y} = 0, y = 0 \tag{A.6}$$

$$\frac{\partial m_{0x}}{\partial y} + \beta_{m0} m_{0x} = \frac{g}{f} \beta_{m0} C_{m0}(x_b - x_a), y = d \tag{A.7}$$

and,

$$B_0 = \frac{1}{D_m}(p + \lambda) \tag{A.8}$$

$$\beta_{m0} = \frac{D_{ey}}{D_m}\gamma_{m0} tanh(\gamma_{m0} h) \tag{A.9}$$

$$\gamma_{m0} = \sqrt{E_0} \tag{A.10}$$

$$E_0 = \frac{1}{D_{ey}} f(p) \tag{A.11}$$

$$\sigma = \sqrt{B_0} \tag{A.12}$$

The solution of equation (A.5) subject to the boundary conditions (A.6, A.7) is:

$$m_{0x} = \frac{(x_b - x_a)\beta_{m0}\cosh(\sigma y)}{\sigma\sinh(\sigma d) + \beta_{m0}\cosh(\sigma d)}\left[\frac{gC_{m0}}{E_0 D_{ey}} - \frac{C_0}{B_0 D_m}\right] + \frac{C_0}{B_0 D_m}(x_b - x_a) \tag{A.13}$$

First spatial moment

The first spatial moment (m_{1x}) is calculated as

$$m_{1x} = i\frac{\partial}{\partial\xi}\overline{C} \quad (\xi = 0, y, p) \tag{A.14}$$

Carrying out the derivative of equations (A.1), (A.2) and (A.3) with respect to ξ, we may find m_{1x} satisfies the following governing equation (A.15) and boundary conditions (A.16, A.17):

$$\frac{\partial^2 m_{1x}}{\partial y^2} - B_0 m_{1x} = -\frac{1}{D_m} v(y) m_{0x}(y) - \frac{1}{2D_m} C_0 (x_b^2 - x_a^2) \tag{A.15}$$

$$\frac{\partial m_{1x}}{\partial y} = 0, y = 0 \tag{A.16}$$

$$\frac{\partial m_{1x}}{\partial y} + \beta_{m0} m_{1x} = \frac{g}{2f} C_{m0}\beta_{m0}(x_b^2 - x_a^2), y = d \tag{A.17}$$

The solution of (A.15) subject to the boundary conditions (A.16, A.17) is:

$$m_{1x} = b_1 e^{-\sigma y} + b_2 e^{\sigma y} + m_{1x}^* \tag{A.18}$$

$$m_{1x}^* = \frac{1}{2\sigma}\{e^{\sigma y}[F_{int}(-\sigma, y) - F_{int}(-\sigma, 0)] + e^{-\sigma y}[F_{int}(\sigma, d) - F_{int}(\sigma, y)]\} \tag{A.19}$$

$$F_{int}(\sigma, y) = -\frac{3v_a}{2D_m}\{\frac{1}{2}A_{m0x}\left[\frac{1}{2\sigma}e^{2\sigma y} - \frac{1}{d^2(2\sigma)^3}e^{2\sigma y}\left((2\sigma y)^2 - 4\sigma y + 2\right) + y - \frac{1}{3d^2}y^3\right] +$$

$$B_{m0x}e^{\sigma y}\left[\frac{1}{\sigma} - \frac{1}{d^2\sigma^3}\left((\sigma y)^2 - 2\sigma y + 2\right)\right]\} - \frac{1}{2D_m\sigma}C_0\left(x_b^2 - x_a^2\right)e^{\sigma y} \tag{A.20}$$

$$b_1 = \frac{r_2 - r_1(\beta_{m0} + \sigma)e^{\sigma d}}{(\beta_{m0} - \sigma)e^{-\sigma d} + (\beta_{m0} + \sigma)e^{\sigma d}} \tag{A.21}$$

$$b_2 = \frac{r_2 + r_1(\beta_{m0} - \sigma)e^{-\sigma d}}{(\beta_{m0} - \sigma)e^{-\sigma d} + (\beta_{m0} + \sigma)e^{\sigma d}} \tag{A.22}$$

$$r_1 = \frac{1}{2\sigma}[F_{int}(\sigma, d) - F_{int}(\sigma, 0)] \tag{A.23}$$

$$r_2 = -\frac{1}{2}\left(1 + \frac{\beta_{m0}}{\sigma}\right)e^{\sigma d}[F_{int}(-\sigma, d) - F_{int}(-\sigma, 0)] + \frac{g}{2f}C_{m0}\beta_{m0}(x_b^2 - x_a^2) \tag{A.24}$$

$$A_{m0x} = \frac{(x_b - x_a)\beta_{m0}}{\sigma\sinh(\sigma d) + \beta_{m0}\cosh(\sigma d)}\left[\frac{gC_{m0}}{E_0 D_{ey}} - \frac{C_0}{B_0 D_m}\right] \tag{A.25}$$

$$B_{m0x} = \frac{C_0}{B_0 D_m}(x_b - x_a) \tag{A.26}$$

Second Spatial Moment

The second spatial moment (m_{2x}) is calculated as

$$m_{2x} = -\frac{\partial^2}{\partial \xi^2}\overline{C} \quad (\xi = 0, y, p) \tag{A.27}$$

Following a similar process to that used to obtain the first spatial moment, carrying out the second order derivative of equations (A.1, A.2, A.3) with respect to ξ yields:

$$\frac{\partial^2 m_{2x}}{\partial y^2} - B_0 m_{2x} = -[2m_{0x}(y) + \frac{2}{D_m} v(y) m_{1x}(y)] - \frac{1}{3D_m} C_0 (x_b^3 - x_a^3) \tag{A.28}$$

$$\frac{\partial m_{2x}}{\partial y} = 0, y = 0 \tag{A.29}$$

$$\frac{\partial m_{2x}}{\partial y} + \beta_{m0} m_{2x} = R_d, y = d \tag{A.30}$$

$$R_d = \beta^*_{m0} m_{0x}(d) - \frac{g}{f^2}\left(\beta^*_{m0} f - 2D_{ex}\beta_{m0}\right) C_{m0}(x_b - x_a) + \frac{g}{3f} C_{m0}\beta_{m0}(x_b^3 - x_a^3) \tag{A.31}$$

$$\beta^*_{m0} = \frac{D_{ex}}{D_m\sqrt{E_0}}[\tanh(\gamma_{m0}h) + \gamma_{m0}h\,\mathrm{sech}^2(\gamma_{m0}h)] \tag{A.32}$$

Accordingly, the solution of (A.28) subject to the boundary conditions (A.29, A.30) is:

$$m_{2x} = d_1 e^{-\sigma y} + d_2 e^{\sigma y} + m^*_{2x} \tag{A.33}$$

$$m^*_{2x} = \frac{1}{2\sigma}\left[e^{\sigma y}\int_0^y \Omega(y) e^{-\sigma y} dy + e^{-\sigma y}\int_y^d \Omega(y) e^{\sigma y} dy\right] \tag{A.34}$$

$$\Omega(y) = -[2m_{0x}(y) + \frac{2}{D_m} v(y) m_{1x}(y)] - \frac{1}{3D_m} C_0 (x_b^3 - x_a^3) \tag{A.35}$$

$$d_1 = \frac{u_2 - u_1(\beta_{m0} + \sigma)e^{\sigma d}}{(\beta_{m0} - \sigma)e^{-\sigma d} + (\beta_{m0} + \sigma)e^{\sigma d}} \tag{A.36}$$

$$d_2 = \frac{u_2 + u_1(\beta_{m0} - \sigma)e^{-\sigma d}}{(\beta_{m0} - \sigma)e^{-\sigma d} + (\beta_{m0} + \sigma)e^{\sigma d}} \tag{A.37}$$

$$u_1 = \frac{1}{2\sigma}\int_0^d \Omega(y) e^{\sigma y} dy \tag{A.38}$$

$$u_2 = -\frac{1}{2}\left(1 + \frac{\beta_{m0}}{\sigma}\right) e^{\sigma d}\int_0^d \Omega(y) e^{-\sigma y} dy + R_d \tag{A.39}$$

Appendix B. Spatial moments of Taylor dispersion model

The solution for the Taylor dispersion model in the Laplace and Fourier domains is presented in equation (31). The spatial moments can be derived accordingly.

Zeroth Spatial Moment

Setting$\xi = 0$ in (31) yields:

$$m_{0x}(p) = \frac{1}{d(p + \lambda) + D_m\beta_{m0}}\left[dC_0(x_b - x_a) + \frac{g}{f} D_m C_{m0}\beta_{m0}(x_b - x_a)\right] \tag{B.1}$$

First Spatial Moment

Directly taking the derivative of (31) with respect to ξ and applying the definition of the first spatial moment results in:

$$m_{1x}(p) = (dC_0 + \frac{g}{f} D_m C_{m0}\beta_{m0})\left[\frac{dv_a(x_b - x_a)}{[d(p + \lambda) + D_m\beta_{m0}]^2} + \frac{x_b^2 - x_a^2}{2[d(p + \lambda) + D_m\beta_{m0}]}\right] \tag{B.2}$$

Second Spatial Moment

Taking the second order derivative of (31) with respect to ξ and applying the definition of the second spatial moment results in:

$$m_{2x} = F_1^{''}(p)F_2(p) + 2F_1^{'}(p)F_2^{'}(p) + F_1(p)F_2^{''}(p) \tag{B.3}$$

where,

$$F_1(p) = \frac{1}{d(p+\lambda) + D_m\beta_{m0}} \tag{B.4}$$

$$F_2(p) = \left(dC_0 + \frac{g}{f}D_m C_{m0}\beta_{m0}\right)(x_b - x_a) \tag{B.5}$$

$$F_1^{'}(p) = \frac{dv_a}{[d(p+\lambda) + D_m\beta_{m0}]^2} \tag{B.6}$$

$$F_2^{'}(p) = \frac{1}{2}(dC_0 + \frac{g}{f}D_m C_{m0}\beta_{m0})(x_b^2 - x_a^2) \tag{B.7}$$

$$F_1^{''}(p) = \frac{1}{[d(p+\lambda) + D_m\beta_{m0}]^3}\{(2dD_f + D_m\beta_{m0}^*)[d(p+\lambda) + D_{m0}\beta_{m0}] + 2d^2v_a^2\} \tag{B.8}$$

$$F_2^{''}(p) = \frac{1}{3}\left(dC_0 + \frac{g}{f}D_m C_{m0}\beta_{m0}\right)(x_b^3 - x_a^3) - \frac{g}{f^2}D_m C_{m0}(\beta_{m0}^* f - 2D_{ex}\beta_{m0})(x_b - x_a) \tag{B.9}$$

References

Abramowitz, M., Stegun, I.A., 1970. Handbook of Mathematical Functions with Formulas, Graphs, and Mathematical tables. Dover, New York.

Barker, J.A., 1982. Laplace transform solutions for solute transport in fissured aquifers. Adv. Water Resour. 5 (2), 98–104.

Berkowitz, B., 2002. Characterizing flow and transport in fractured geological media: A review. Adv. Water Resour. 25, 861–884.

Bloechle, B.W., 2001. On the Taylor Dispersion of Reactive Solutes in a Parallel-Plate Fracture-Matrix System. Ph.D. thesis. Department of Applied Mathematics, University of Colorado, Boulder, Colorado, p. 266.

Boschan, A., Ippolito, I., Chertcoff, R., Auradou, H., Talon, L., Hulin, J.P., 2008. Geometrical and Taylor dispersion in a fracture with random obstacles: An experimental study with fluids of different rheologies. Water Resour. Res. 44, W06420. https://doi.org/10.1029/2007WR006403.

Brabazon, J.W., Perfect, E., Gates, C.H., Bilheux, H.Z., Tyner, J.S., McKay, L.D., Horodecky, B.B., 2019. Rock fracture sorptivity as related to aperture width and surface roughness. Vadose Zone J. 18, 180156 https://doi.org/10.2136/vzj2018.08.0156.

Chen, C.S., 1986. Solutions for radionuclide transport from an injection well into a single fracture in a porous formation. Water Resour. Res. 22 (4), 508–518. https://doi.org/10.1029/WR022i004p00508.

Chen, K.W., Zhan, H.B., 2018. A Green's function method for two-dimensional reactive solute transport in a parallel fracture-matrix system. J. Contam. Hydrol. 213, 15–21.

Clark, M.M., 2009. Transport Modeling for Environmental Engineers and Scientists, 2nd ed. Wiley, Hoboken, NJ.

de Hoog, F.R., Knight, J.H., Stokes, A.N., 1982. An improved method for numerical inversion of Laplace transforms, S.I.A.M. J. Sci. and Stat. Comp. 3, 357–366.

Deng, H., Ellis, B., Peters, C.A., Fitts, J.P., Crandall, D., Bromhal, G.S., 2013. Modifications of carbonate fracture hydrodynamic properties by CO2-acidified brine flow. Energy Fuels 27 (8), 4221–4231.

Detwiler, R.L., Rajaram, H., Glass, R.J., 2000. Solute transport in variable-aperture fractures: An investigation of the relative importance of Taylor dispersion and macrodispersion. Water Resour. Res. 36 (7), 1611–1625.

Ellis, B., Peters, C., Fitts, J., Bromhal, G., McIntyre, D., Warzinski, R., Rosenbaum, E., 2011. Deterioration of a fractured carbonate caprock exposed to CO2-acidified brine flow, Greenhouse Gases. Sci. Technol. 1, 248–260. https://doi.org/10.1002/ghg.025.

Fischer, H.B., List, E.J., Koh, R.C.Y., Imberger, J., Brooks, N.H., 1979. Mixing in Inland and Coastal Waters. Academic, San Diego, Calif.

Goltz, M.N., Huang, J., 2017. Analytical Modeling of Solute Transport in Groundwater - Using Models to Understand the Effect of Natural Processes on Contaminant Fate and Transport. Wiley, Hoboken, NJ, p. 2017.

Goltz, M.N., Oxley, M.E., 1991. Analytical modeling of aquifer decontamination when transport is affected by rate-limited sorption. Water Resour. Res. 27 (4), 547–556.

Grisak, G.E., Pickens, J.F., 1981. An analytical solution for solute transport through fractured media with matrix diffusion. J. Hydrol. 52 (1–2), 47–57.

Hollenbeck, K.J. (1998). INVLAP.m: A MATLAB function for numerical inversion of Laplace transforms by the de Hoog algorithm, http://www.isva.dtu.dk/staff/karl/invlap.html.

Houseworth, J.E., Asahina, D., Birkholzer, J.T., 2013. An analytical model for solute transport through a water saturated single fracture and permeable rock matrix, Water Resour. Res. 49, 6317–6338. https://doi.org/10.1002/wrcr.20497.

Kittilä, A., Jalali, M., Saar, M.O., Kong, X.Z., 2020. Solute tracer test quantification of the effects of hot water injection into hydraulically stimulated crystalline rock. Geotherm. Energy 8, 17. https://doi.org/10.1186/s40517-020-00172-x.

Li, X., Li, D., Xu, Y., Feng, X., 2020. A DFN based 3D numerical approach for modeling coupled groundwater flow and solute transport in fractured rock mass. Int. J. Heat Mass Transf. 149 https://doi.org/10.1016/j.ijheatmasstransfer.2019.119179.

Li, C., 2016. Dynamic Modeling of the Geological CO_2 Storage in Fractured Aquifers—Application to the Ordos Basin CCS Project. PhD thesis. Faculty of Engineering and Information Technologies, The University of Sydney, Sydney, Australia.

Liu, L., Neretnieks, I., Shahkarami, P., Meng, S., Moreno, L., 2018. Solute transport along a single fracture in a porous rock: a simple analytical solution and its extension for modeling velocity dispersion. Hydrogeol. J. 26, 297–320. https://doi.org/10.1007/s10040-017-1627-8.

Maloszewski, P., Zuber, A., 1985. On the theory of tracer experiments in fissured rocks with a porous matrix. J. Hydrol. 79, 333–358.

Maloszewski, P., Zuber, A., 1990. Mathematical modeling of tracer behavior in short-term experiments in fissured rocks. Water Resour. Res. 26 (7), 1517–1528.

Nardin, M., Perger, W.F., Bhalla, A., 1992. Algorithm 707: CONHYP, A numerical evaluator of the confluent hypergeometric function for complex arguments of large magnitudes. ACM Trans. Math. Softw. 18, 345–349.

National Research Council (NRC), 1996. Rock Fractures and Fluid Flow: Contemporary Understanding and Applications. The National Academies Press, Washington, DC.

Neretnieks, I., 1980. Diffusion in the rock matrix: An important factor in radionuclide retardation. J. Geophys. Res. 85, 4379–4397.

Neretnieks, I., 2017. Solute Transport in Channel Networks with Radial Diffusion from Channels in a Porous Rock Matrix, SKB technical report R-15-02. Svensk Kärnbränslehantering AB, Sweden.

Polyanin, A.D., Zaitsev, V.F., 1995. Handbook of Exact Solutions for Ordinary Differential Equations. by CRC Press Inc.

Roubinet, D., de Dreuzy, J.-R., Tartakovsky, D.M., 2012. Semi-analytical solutions for solute transport and exchange in fractured porous media. Water Resour. Res. 48, W01542. https://doi.org/10.1029/2011WR011168.

Roux, S., Plouraboue, F., Hulin, J.P., 1998. Tracer dispersion in rough open cracks. Transp. Porous Media 32, 97–116.

Schäfer, T., Geckeis, H., Bouby, M., Fanghänel, T., 2004. U, Th, Eu and colloid mobility in a granite fracture under near-natural flow conditions, Radiochim. Acta 92, 731–737.

Sudicky, E.A., Frind, E.O., 1982. Contaminant transport in fractured porous media: Analytical solutions for a system of parallel fractures. Water Resour. Res. 18 (6), 1634–1642.

Tang, D.H., Frind, E.O., Sudicky, E.A., 1981. Contaminant transport in fractured porous media: Analytical solution for a single fracture. Water Resour. Res. 17 (3), 555–564.

Taylor, G., 1953. Dispersion of soluble matter in solvent flowing slowly through a tube. Proc. R. Soc. A 219, 186–203.

Vandersteen, K., B. Busselen, K. Van Den Abeele, and J. Carmeliet (2003) Quantitative characterization of fracture apertures using microfocus computed tomography, Geological Society, London, Special Publications, 215, 61-68, 1 January 2003.
Wang, L., Cardenas, M.B., Deng, W., Bennett, P.C., 2012. Theory for dynamic longitudinal dispersion in fractures and rivers with Poiseuille flow. Geophys. Res. Lett. 39, L05401.
Zhou, R.J., Zhan, H.B., 2018. Reactive solute transport in an asymmetrical fracture-rock matrix system. Adv. Water Resour. 112, 224–234.
Zhou, R.J., Zhan, H.B., Chen, K.W., 2017. Reactive solute transport in a filled single fracture-matrix system under unilateral and radial flows. Adv. Water Resour. 104, 183–194.
Zhu, Y.H., Zhan, H.B., 2018. Quantification of solute penetration in an asymmetric fracture-matrix system. J. Hydrol. 563, 586–598.
Zhu, Y.H., Zhan, H.B., Jin, M.G., 2016. Analytical solutions of solute transport in a fracture-matrix system with different reaction rates for fracture and matrix. J. Hydrol. 539, 447–456.